A Fully Spectral 3D Time-Domain Model for Second-Order Simulation of Wavetank Experiments. Part B: Validation; Calibration versus experiments and Sample Applications

F. Bonnefoy, D. Le Touzé, P. Ferrant

A fully-spectral 3D time-domain model for second-order simulation of wavetank experiments. Part B: Validation, calibration versus experiments and sample applications

Félicien Bonnefoy*, David Le Touzé, Pierre Ferrant

Laboratoire de Mécanique des Fluides, Ecole Centrale de Nantes, 1 rue de la Noë, BP 92101, 44321 NANTES Cedex 3, France

A 3D second-order numerical wavetank (NWT) model, *SWEET*, is presented. In the first part (A) of the paper [Bonnefoy F, Le Touzé D, Ferrant P. A fully-spectral 3d time-domain model for second-order simultion of wavetank experiments. Part A: Formulation, implementation and numerical properties. Appl Ocean Res 2005 [submitted for publication]. doi:10.1016/j.apor.2006.05.004], the fully-spectral formulation we employ has been detailed, and the numerical properties of the model analyzed. In the present part (B), careful validation by comparison to analytical and experimental results is first reported. Thanks to the efficiency of the proposed spectral method, the shortest wavelengths in the wavetank can be accounted for with moderate computational times. The consequent possibilities are illustrated here for the following 2D and 3D complex wave-pattern simulations, with experimental comparisons: wave-packet and geometric focusing cases, directional wavefields, long-time evolutions of irregular waves. The numerical model features all the physical characteristics of a wavetank (snake wavemaker, experimentally-calibrated absorbing zone, etc.). Its usefulness to help preparing and analyzing experiments is shown in relation to some key practical requirements: e.g. quality and evolution of the usable test zone and usability of enhanced wavemaker motions.

Keywords: 3D NWT; Second order; Spectral methods; FFTs; Directional wavemaker; Usable test zone; Experimental-aid tool; Focusing; 3D realistic wavefields

0. Introduction

In the first part (A) of the present paper [1], a methodology and the corresponding numerical algorithm have been described to simulate, in the time domain at second order, the whole wave generation and propagation process in a wavetank. This three-dimensional NWT, named *SWEET* is based on a fully-spectral method first presented in [2] and significantly enhanced since then. The proposed spectral resolution has been detailed in Part A [1], and the expected accuracy, quick-convergence and run-time properties of the model have been illustrated. The exhibited efficiency of this approach, with the problem solved by means of FFTs only, led to the conclusion that simulations of 3D realistic wave patterns at moderate cost were possible, including the shortest wavelengths present in the wavetank. Furthermore, the development of wavemaker motions similar to the experimental ones have extended the applicability of the model to complex sea-states; this will be illustrated in the present part (B) of the paper.

In this part, a careful validation by comparison to a dedicated semi-analytical theory developed by Bonnefoy et al. [3] is first presented (see Section 1). This second-order analytical solution provides the stationary evolution of the wavefield in a semi-infinite three-dimensional wavetank; it includes the actual wavemaker motion. Further validation of the model is made against various experimental results, in each case showing very good agreement. These comparisons are thoroughly analyzed to understand up to what extent, in terms of time evolution and nonlinearities, the model is able to reproduce a real basin. The 2D and 3D complex wave-pattern cases investigated as examples in this Part B include: wave-packet and geometric focusing events; the generation of a focused directional irregular wavefield; and long-time evolutions of irregular waves (see Sections 3.2 and 3.4). The variety of the

* Corresponding author. Tel.: +33 240 371 631; fax: +33 240 372 523.
E-mail addresses: Felicien.Bonnefoy@ec-nantes.fr (F. Bonnefoy), David.LeTouze@ec-nantes.fr (D. Le Touzé), Pierre.Ferrant@ec-nantes.fr (P. Ferrant).

model possibilities is also illustrated through an example of a pre-design study (see Section 3.3).

In order to develop a tool facilitating the preparation and analysis of experimental tests, all the characteristics of the physical wavetank have been included in the model (see [1]). In particular, a sustained effort has been made since [2] to improve the wave generation process; only regular oblique waves could be generated at the time of the latter article. Here, the arbitrary shape and motion of the 3D wavemaker is reproduced, and numerical and experimental wavemaker motions are created in identical ways, using a shared input process (see Section 2.1). Furthermore, the numerical absorption has been designed and calibrated through comparison with dedicated experiments in the basin, to provide absorbing features similar to the ones of the real wavetank beach (see Section 2.2).

In order to perform useful experiments one has to know the area in the basin where the measured wavefield will be close enough to the prescribed field, i.e. the usable test zone. Indeed, due to side-wall reflections, nonlinear generation and propagation processes, and partial reflection on the absorbing beach, the wave pattern realised in the basin differs significantly from that prescribed, at least over parts of its surface. The knowledge of the usable test-zone extent, quality and time evolution is therefore vital, but it is difficult to evaluate and optimize it heuristically. As shown by theoretical linear studies, the chosen wavemaker motion plays a dominant role and can be optimized to enlarge and shift the test zone. After the simple 'snake principle' of Biésel [4], Dalrymple [5] proposed an enhanced motion taking advantage of side-wall reflections (from which more elaborate methods have then been derived, see e.g. Boudet and Pérois [6]). However, all these solutions are based on first-order frequency domain theory. The present model, including both unsteady aspects and second order effects, offers much wider possibilities of analysis, showing the limits of these linear techniques (see Section 3.1 and [2]). Finally, among other examples of the aid to wavetank experiments provided by our model *SWEET*, it permits one to optimize the time ramp applied to the real wavemaker motion at the start (see Section 2.1).

1. Validation with analytical solutions

For moderate-steepness wavefields, second-order analytical solutions can be derived in some particular situations, and used to verify time-domain numerical methods. In this way, the core of the present spectral model (the basin without wavemaker) has been successfully compared to a 2D second-order analytical solution by Cointe et al. [7], in the case of the free evolution of an initial constant-slope free surface. Very close agreement has been found regarding both the modal amplitudes and the free surface elevations, and the expected decrease rate of the modal amplitudes has been recovered (see [8]). Furthermore, the accuracy levels reached and the computational costs exhibited have been acknowledged to be largely favorable with respect to a Boundary-Element Method solution [9] of the same problem.

The present NWT has then been compared to a second-order frequency-domain analytical solution of the directional wavemaker problem, which readily provides the steady state for a regular wavefield. In two dimensions, numerous analytical works are available (see e.g. Hudspeth and Sulisz [10], and Schäffer and Steenberg [11] for a review), and the comparisons we achieved with [10] turned out to be very satisfactory [8]. In three dimensions, Schäffer and Steenberg [11] have dealt with multidirectional waves, but in a basin without sidewalls and only with the snake principle as the wavemaker control law. Li and Williams [12] have treated the case of regular waves in a basin with perfectly reflective sidewalls and with the snake principle. The work presented in Bonnefoy et al. [3] is an extension of the latter to more complex control laws such as the Dalrymple method [5], and this is used here as reference with which to compare the output of our NWT. This analytical solution is briefly described in Appendix A. The comparison is made possible by the presence of the absorbing layer in the NWT, equivalent to the radiation condition used in the analytical solution.

The basin geometry taken as the example in the following is that of the ECN wavetank (unless otherwise mentioned): a length of 50 m, a width of 30 m and a depth h of 5 m. Fig. 1 shows the comparison at first (top) and second (bottom) orders, for the generation of a regular wave of frequency 0.56 Hz and direction 20° from the main direction, using the Dalrymple control law with a 20 m target distance (see Section 3.1 and Appendix B). In the simulation, 256×64 modes are used on the free surface, and 64×64 on the wavemaker. One time-step takes approximately 2 s CPU on a 3 GHz-Xeon single-processor PC, so that the computation of the 90 s real-time shown in Fig. 1 is completed in 2 h 30 min. In the left part of the figure, one sees the free surface elevations obtained numerically at $t = 50T$. The wavemaker is located at the top left boundary, and the beach in the bottom right part; the wave propagates from top to bottom. In order to correctly compare our numerical model to the frequency-domain solution, the output of the model is taken at a steady state, when both the wave front and the free-wave front have reached the absorbing zone. In the right part are plotted the errors relative to the maximum elevation in the basin, at each order (the errors in the absorbing zone, after $x/h = 8$, are irrelevant since the analytical solution does not take into account any absorption). We can observe that the error at first order is low and relatively homogeneous. Disregarding the absorption zone, the mean relative error over the basin free surface is 0.3%. The present NWT is therefore accurate on the whole domain of calculation, and in particular, it correctly reproduces the presence of both the sidewalls (reflections) and the wavemaker (evanescent modes).

At second order, the required wavelength is much shorter and would ideally require a finer resolution than used at first order. However, our model uses the same resolution at both orders, so we obtain higher error levels at second order, as shown in the bottom right part of Fig. 1. The mean error over the wavetank surface is nonetheless 1.7% only. At a more detailed level, one can observe some spurious second-order free waves in the tank, especially along the wall at $y/h = 0$. Their small wavelength is approximately $\lambda/4$ and corresponds to the 80th mode of the spectral expansion. The ratio of the corresponding

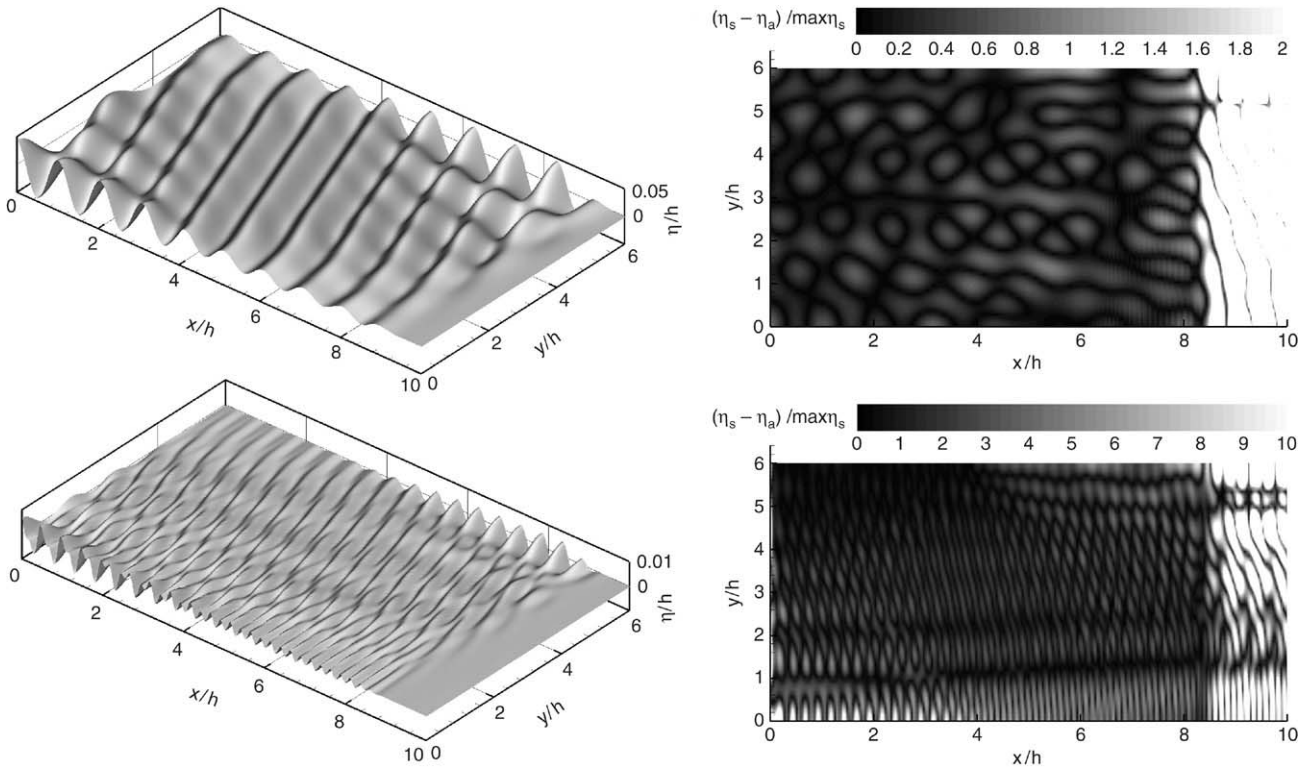

Fig. 1. Left: simulated elevations at $t = 50T$. Right: errors relative to a frequency-domain solution (top: first order; bottom: second order).

mode over the total number of modes used is thus only 0.3 in the x-direction, whereas it was 0.08 at first order. The difference in the measured mean errors between first and second orders is therefore consistent.

2. Experimental calibration of the NWT

2.1. Wavemaker

With the aim of reproducing as closely as possible the generation abilities of the physical basin, great care has been taken to model the generation process within our NWT model *SWEET*. In particular, as detailed in Part A [1], the snake wavemaker geometry is fully reproduced in our model, with the only additional assumption of its continuity along the y-direction. Other geometries such as a piston are also implemented.

One of the issues for the model validation and usability is to be able to easily compare the numerical results with experimental data collected in the real tank. The easiest way to do so is to drive the two wavemakers in the same way. Keys to this procedure are the experiment description language, *Wave*, and its associated compiler, *Ocean*. This language was developed by Edinburgh Designs, the wavemaker builder, solely for the purpose of wavetank research and experimentation, and is thus optimized for wave generation. The basic principle is to describe the wavefield in terms of linear wave components, which are transformed into wavemaker position components by the appropriate linear transfer function. The *Wave* language includes a set of predefined spectra (Pierson–Moskowitz, JONSWAP, etc.), directional spreading ($\cos^n(\theta - \theta_o)$ or $\cos^{2n}(\theta - \theta_o)/2$) and several built-in functions with specific purposes such as focusing. It also allows reading an external data file containing the characteristics of the desired wave components. Two control laws were selected for the case of oblique regular waves: the snake principle [4] which was the only control originally provided in *Ocean*, and the Dalrymple method [5] which we have implemented, and which is now used in a routine way (see also 3.1 and Appendix B). After describing and compiling an experiment using *Wave* and *Ocean*, one output is a wavemaker-position file which is used to control, in real-time, the individual physical flaps by position feedback; another is a data file in which are stored the directional frequency components. The latter is used as input for the numerical wavemaker control. In *SWEET*, the wavemaker position $X(y, z, t)$ is therefore evaluated at each required time using exactly the same procedure as in *Ocean* (i.e. linear transfer function, snake principle or Dalrymple method, and sum over the components).

As mentioned in [1], the efficiency of the time ramp superimposed on the wavemaker motion at the start is important, to avoid spurious transient loads on the wavemaker itself, and transient waves propagating across the basin during the tests. In the ECN physical wavetank, this ramp was originally prescribed as linear and of duration 3 s. With a view to testing its efficiency we have studied in our model *SWEET* the effect of the two parameters: shape and duration of the ramp. The result for two-dimensional regular waves is plotted in Fig. 2, which shows the time history of the elevation at a probe located a few wavelengths away from the wavemaker. One can note that the dominant parameter

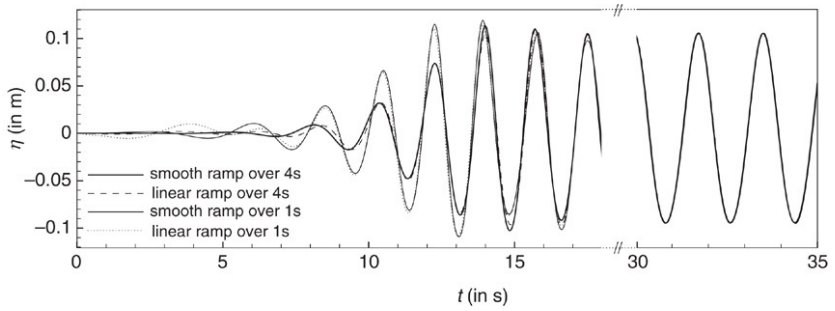

Fig. 2. Influence on the wave front of the duration and smoothness of the ramp superimposed to the wavemaker motion at start. Smooth ramp shape over T_r: $(3u^2 - 8u + 6)u^2$ with $u = t/T_r$.

affecting the generated wave-train shape is the duration of the ramp. A longer ramp indeed reduces the amplitude of the first waves in the front, and in particular of the highest ones; this can be interesting to avoid unwanted breaking of the front when generating a non-breaking wave pattern. Moreover, using a smooth shape for the ramp (leading to a C^1 motion between $t = 0^-$ and $t = T_r^+$) helps attenuating the first waves to reach the probe, whose wavelengths and velocities are much greater than those of the prescribed regular wave. These unwanted long modes being therefore less excited, they need less absorption by the physical beach and the corresponding numerical absorbing zone. This is eventually compatible with the low performance of the two absorbing zones for long wavelengthes (see Molin [13] and Bonnefoy [14]). Thanks to this numerical investigation using *SWEET*, more efficient ramp formulations are now implemented in the ECN wavetank.

2.2. Absorbing layer

The numerical model includes a damping zone to absorb the waves at the end of the basin (see [1]). The damping term $\nu(\vec{x})$ in the equation $p_a = \rho\,\nu(\vec{x})\,\vec{\nabla}\phi.\vec{n}$ (on $z = \eta$) has to be chosen carefully, for the numerical absorbing zone to match the properties of the beach of the ECN wavetank. For this basin geometry, the damping term is non-zero only near the wall opposite to the wavemaker as shown in Part A [1], Figure 5; but it can generally be more complicated (see Fig. 9). Its mathematical expression is chosen here as a third-order polynomial: $\nu(\vec{x}) = 0$ if $x < x_o$ and $\alpha u^2(3 - 2u)$ elsewhere with $u = (x - x_o)/L_b$ and $L_b = L_x - x_o$. This expression gives satisfactory smoothness properties at the boundaries of the damping zone, and the damping term simply depends on two parameters, the zone length L_b and its strength α.

The physical beach has been studied through a series of dedicated experiments, and the reflection coefficient was found in the range of 5%–10% in amplitude for most of the tested frequencies. The reflection of the numerical absorbing zone has then been investigated by generating successively several 2D linear waves, covering the range of useful wavelengths. After a Fourier analysis at the wavemaker frequency, the method of Mansard and Funke [15] with three probes gives us the incident a_{inc} and reflected a_{ref} amplitudes, that we use to calculate a reflection coefficient in amplitude given by $C_r = a_{ref}/a_{inc}$.

Two preliminary studies are then needed and consist respectively in varying one of the two design parameters while the second is fixed, at a given wavelength λ (taken equal to the depth here). Using a damping length L_b equal to two wavelengths and varying the strength, we observed that the reflection coefficient is almost constant once the strength is above a given threshold α_c ($\alpha_c = 0.2$ for the particular wavelength and damping length tested). Below this threshold, reflection coefficients rapidly increase; low values of α are thus inadequate to accurately control the reflection. Using a strength above the threshold, and this time varying L_b, we observed the expected smooth decrease of the reflection coefficient as the length increased, giving us the opportunity to correctly tune the behaviour of the numerical damping zone. A 5% coefficient in amplitude is for example obtained for $L_b = h$ with $\alpha = 0.4$. Eventually, once the two parameters have been chosen ($L_b = h$ and $\alpha = 0.4$), we are able to estimate the evolution of the reflection coefficient for the range of frequencies used in the basin, as shown in Fig. 3. One can notice that within the mid frequency range, the values of the reflection coefficient are in good agreement with the experimental ones, between 5 and 10%. For the highest frequencies however, the waves are much better absorbed in the NWT than in the experiments. For these high frequencies, the relative length of the damping zone compared to the wavelength increases. Whereas in the physical basin, the absorption, which mostly happens by breaking, is almost unaffected by this variation, in the model however the performance of the damping zone is closely linked to the damping length/wavelength ratio, and increases with it. For the low frequency range, one can observe the relatively high

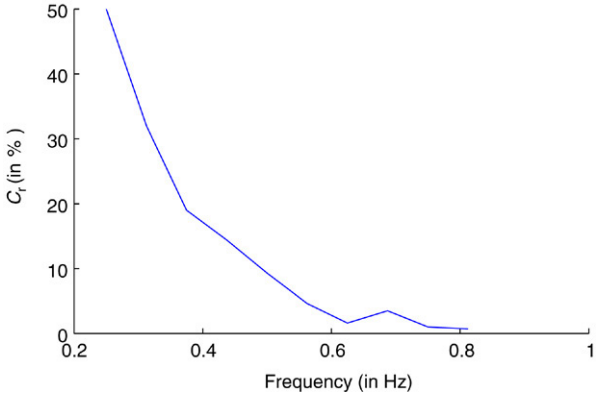

Fig. 3. Reflection coefficient with $L_b = h$ and $\alpha = 0.4$.

reflection coefficient in the numerical model.[1] This behaviour confirms the observation of Molin [13] that the long modes are hardly damped in regular-wave experiments.

3. Sample applications

The model having been validated and tuned to match the experimental generation and absorption properties, its capabilities can be investigated and quantified, as well as its usefulness to assist wavetank experiments. In the present section, the possibilities offered by the model are illustrated on typical example cases including some comparisons with experimental results.

3.1. Usable test zone investigation: An example aid to experiments

As a tool assisting experiments, the model has been used to analyze *a priori* the wavefield quality in the basin for a given wavemaker motion. The knowledge of the extent and time evolution of this usable zone is a major issue when conducting experiments in the wavetank, and the wavemaker control law is known to have a decisive influence on it. A classical study in the literature (see Boudet and Pérois [6]) is the determination of the usable test zone for regular oblique waves. However, this kind of study is based on both linear and steady-state assumptions. Our model is therefore suitable to assess up to what extent the conclusions of these linear theories remain valid when nonlinear and unsteady effects are accounted for (see [2]). Nonetheless, the presented model has been considerably enhanced since [2], as it has been mentioned in Part A [1]: (a) the efficient improved resolution [1] now employed (fully FFT-based) permits correctly describing the shortest wavelengths in the tank; (b) substantial efforts have been made to make the numerical model match with the physical basin characteristics (see Section 2); (c) the model convergence and accuracy properties have been verified and quantified (see Part A [1] and Section 1). Long-time evolutions of complex 3D wavefields can thus now be calculated at moderate CPU costs and the validity of the results confirmed by experimental comparisons (see following sections), while this kind of simulation was beyond practical applicability at the time of the study made in [2]. Nonetheless, the conclusions of the latter detailed study have been globally confirmed when it has been redone with the new model presented here. This updated study, realized with about 10 times as many modes as in [2], is therefore only partly and briefly reported here.

In this study, both the snake principle and the Dalrymple method have been applied to the wavefield described in Section 1 ($f = 0.56$ Hz, $\theta = 20°$), with $X_d/h = 4$ for the latter technique (see Appendix B). Fig. 4 shows a 3D view of the linear wavefield for the snake principle at time $t = 19T$ when the wave front reaches the wall opposite to the wavemaker: the wavefield is therefore totally free of reflection at the beach. This Fig. 4 is to be compared with the top left view in Fig. 1 obtained with the Dalrymple method. Fig. 5 plots the corresponding wave amplitude at the wave frequency, evaluated over one period by Fourier analysis and normalized by the target amplitude. The snake principle (left hand figure) gives a poor-quality usable test zone, limited to a triangle (in white) in front of the wavemaker. Besides, a strong transverse stationary wave due to reflections appears close to the sidewall $y/h = 6$, whereas close to the opposite sidewall $y/h = 0$ the diffraction is dominant, resulting in low wave amplitude. The amplitude map for the Dalrymple method (right hand figure) shows a much larger usable zone, with its characteristic diamond shape (in white) around the position $x = X_d$. The gain allowed by this method over the snake principle is therefore obvious at first order, in accordance with the frequency-domain linear-theory predictions of Dalrymple [5].

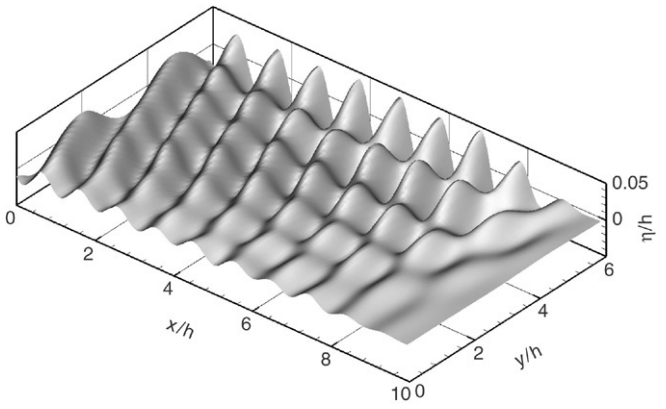

Fig. 4. Regular oblique waves generated with the snake principle.

In Fig. 6 is plotted the second-order double-frequency amplitude when using the Dalrymple method. Normalization is made by the deep-water second-order Stokes amplitude $ka^2/2$. The bound waves at second order being closely related to the first-order ones and the latter being almost unidirectional and of constant amplitude in the diamond-shape first-order usable test zone, a similar diamond pattern with constant amplitude is expected at second order. In Fig. 6 however, the observed waves are more like an interference pattern over the whole surface of the basin, and reveals that the second-order wavefield contains superimposed spurious waves. Therefore, the elaborated Dalrymple method leads to a very poor quality at second order. These parasitic waves, known as free waves[2] and due to the second-order nonlinearities of the generation process, are also clearly visible in Fig. 1, in particular close to the sidewall $y/h = 0$. Their amplitude, direction and wavelength differ from the bound waves, hence leading to the interference pattern observed earlier.

It is worth noting that, since our model is formulated in the time domain we can follow the evolution of the wavefield.

[1] The matching between the absorbing layer and the experimental beach can be refined by applying different damping functions ν to separate wavenumber ranges.

[2] An analytical prediction of the spurious free waves for oblique waves in a wave basin with reflective sidewalls and elaborated wavemaker motions can be found in Bonnefoy et al. [3]. A future paper will show how this prediction can be applied in both the NWT and in experiments to construct a wavemaker motion that cancels the generation of the spurious waves.

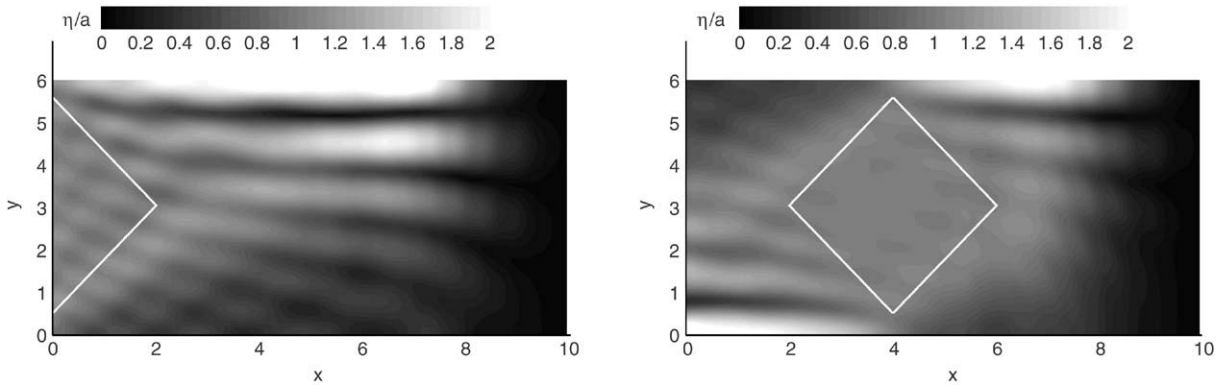

Fig. 5. Usable test zone at first order after 19 periods (left: snake principle, right: Dalrymple method).

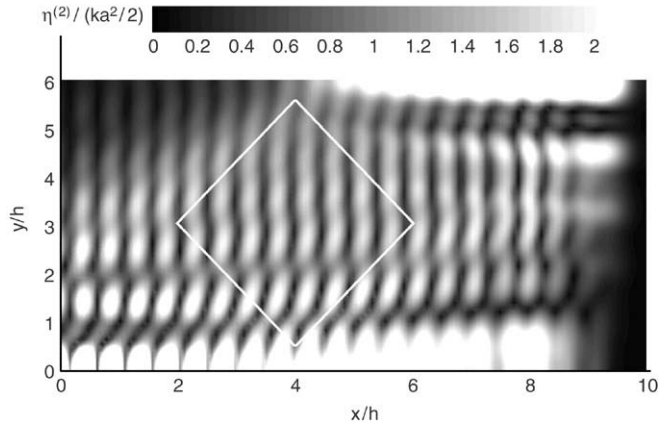

Fig. 6. Usable test zone at second order after 38 periods, using the Dalrymple method.

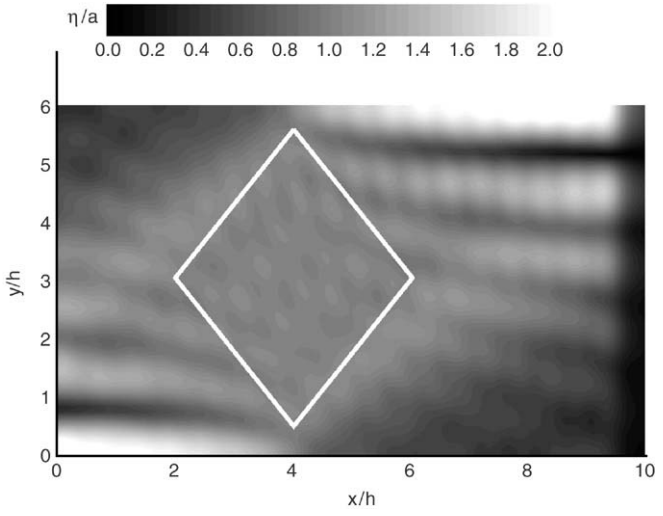

Fig. 7. Usable test zone at first order after 57 periods, using the Dalrymple method.

Multiple reflections on the beach and on the sidewalls can of course be expected to alter the wave quality. Fig. 7 shows an amplitude map of the free surface after 57 periods of wave generation (during which the wave front crosses three basin lengths). One can notice the drop in quality after several reflections: compared to the right part of Fig. 5 the transverse stationary pattern is more pronounced in the lower-left and upper-right corners, where the reflections on sidewalls required by the Dalrymple method occur. Consequently, the usable zone is of smaller extent in the main direction of the basin.

3.2. Accurate reproduction of moderate-steepness events

The adopted second-order description of the wavefield is accurate for modelling waves of moderate steepness in the basin. A verification of our model *SWEET* in that sense has been carried out the case of 2D focused wave packets, by comparison with experimental results. Following the methodology adopted by Baldock et al. [16] (see Appendix C), one can investigate some nonlinear properties of the experimental wave packet which can then be compared to the numerical results. In particular, for wave groups of moderate steepness, the odd elevation η_{odd} extracted from the experimental signals is expected to correspond to the linear wavefield. The even elevation η_{even} is assumed to be an estimation of the second-order field. Comparisons can thus be drawn between the NWT and the adequately separated nonlinear experimental components.

The wave groups studied here are characterized by a wave height of 0.3 m for a 7.7 m peak wavelength (i.e. 3.9% steepness). This steepness is chosen to be high enough to obtain an accurate measurement of the low-amplitude second-order elevation, but not too high to avoid sensible higher-order effects. In the top part of Fig. 8, one can observe that the odd elevation and the linear numerical result superimpose well. In the bottom part, the even elevation and the second-order result also show a good overall agreement. Some discrepancies can be noticed however, which are attributed to higher-order nonlinear effects. One effect of the third-order nonlinearities is indeed the modification of the phase velocity, as shown in Bonnefoy [14]. In the odd elevation, the phases of the different wave components are thus modified at the focusing point, and the superimposition of these time-shifted components leads to a wave packet elevation different from the linear one. This third-order phase velocity modification is also present in the even elevation, as shown in Appendix C, since this elevation represents the bound waves at second order.

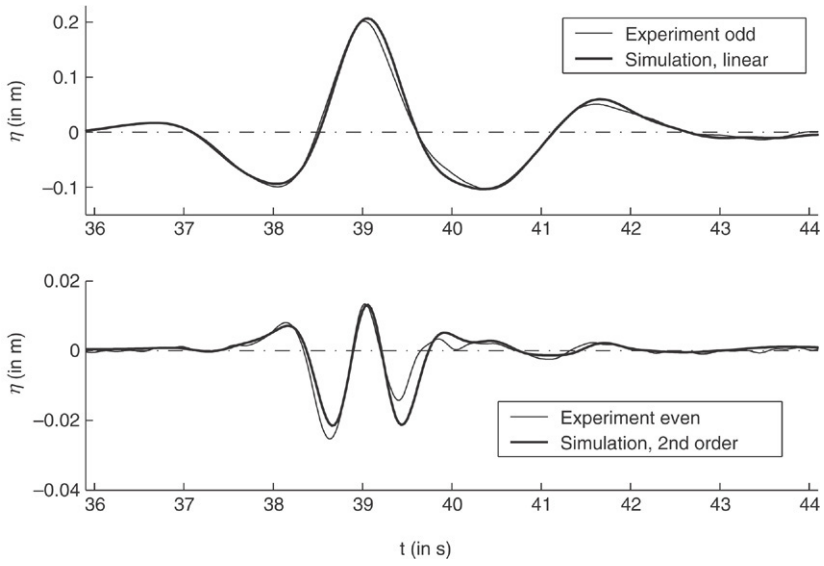

Fig. 8. Comparison between experimental and numerically-predicted elevations.

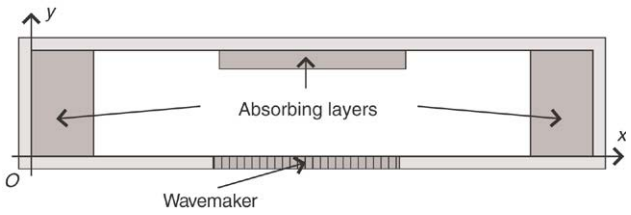

Fig. 9. Sketch of the absorbing layers used in the towing tank for the pre-design study (top view).

3.3. Predesign tool

The formulations we have adopted for both the generation process and the damping zone allow one to easily account for complex wavemaker and beach geometries. The present model has thus been used as an aid to the design of new configurations of a wave basin. The pre-design study we conducted consisted in investigating the addition of a lateral wavemaker in an existing towing tank. The tank's owners were willing to install a wavemaker in the middle of a sidewall, occupying about a fifth of it, and which would face an absorbing beach on the opposite sidewall. They provided required specifications regarding the wavemaker geometry, beach performance and wave test cases, which were all included in the NWT. Fig. 9 shows a top view of the numerical domain we adopted. As the area of interest is limited to the portion of the towing tank surrounding the lateral wavemaker, we used a reduced-length basin ended by two 'powerful' numerical absorbing zones to avoid any reflection. The performance of the prescribed absorbing layer opposite to the wavemaker however, was set to fit the specifications. Fig. 10 illustrates some of the linear simulations that have been carried out with regular waves. The requested results we produced dealt with the time evolution of the wave amplitude on the basin surface, and the monitoring of the linear excitation of the basin natural modes (which can be achieved directly in our spectral method, through the study of the modal-amplitude evolution). The latter monitoring gives a hint of the spurious modes excited

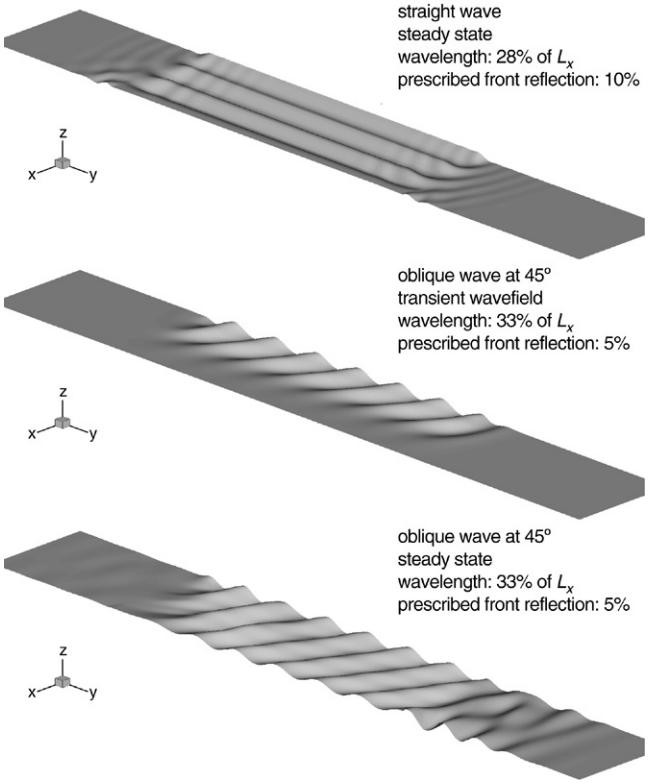

Fig. 10. Wave generation with a partial lateral wavemaker in a towing tank.

by transients, as well as of the remaining wavefield once the wavemaker is stopped and the generated waves are absorbed by the beach.

3.4. Complex wave fields

The first example simulation of complex wavefield deals with a geometric focusing case, i.e. regular waves converging toward the middle of the basin. The wavemaker motion is built by superimposing $N = 11$ wave components of the same

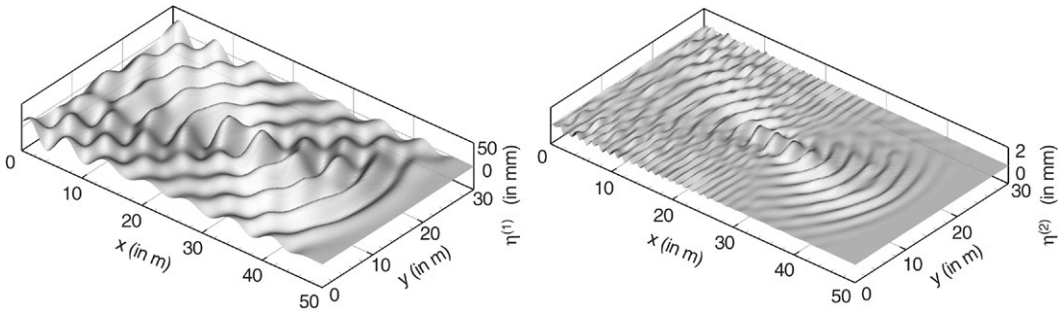

Fig. 11. Geometric focusing: first (left) and second (right) order elevations.

wavelength 5 m, the same amplitude a and directions equally spread between $-45°$ and $+45°$ around the main axis. Initial phases are adjusted so that the individual waves become in phase at the middle of the basin. The linear steepness at the focusing point is defined as $\varepsilon = 2A/\lambda$, where $A = Na$ is the total amplitude at the focusing point, and this is set to $\varepsilon = 2\%$. The Dalrymple method is used for each component, with $X_d/h = 5$. The left part of Fig. 11 shows the first-order elevation at $t = 22T$, and the right part the corresponding second-order elevation. The wavemaker is located at the top-left side of the basin. Although not reproduced here, the same simulation but with the snake principle shows lower crests and a focusing packet which is more spread in the transverse direction. Fig. 12 gives the elevation η/A at first-plus-second orders, measured at a wave probe located at the focusing point. The elevations obtained with both the snake principle and the Dalrymple method are plotted, as well as three horizontal lines representing the average amplitudes for, from top to bottom: the Dalrymple-method simulation, the linear analytical result ($\eta/A = 1$), and the snake-principle simulation. The snake principle is seen to be inadequate for such a wavefield; the Dalrymple method exhibits conversely the correct behaviour. A slight discrepancy can however be seen between the Dalrymple-method probe and the linear theory. In the former, the second-order component (shown in the right part of Fig. 11) is included but it is not high enough to explain the differences; and as discussed in Section 1, the 128×64 (free surface) and 64×64 (wavemaker) meshes used here guarantee a good accuracy at both orders. This difference can be attributed mainly to the Dalrymple method which provides a slightly imperfect reproduction of the oblique components for the very high angles used here. Further, in the second-order elevation, one can note that the short-wavelength free-wave pattern presents an almost constant amplitude in the transverse direction. This amplitude is about one fifth of the second-order bound amplitude at the focusing point, and is thus not negligible. This free-wave contamination of the wavefield would also be evident in the corresponding experiment (conducted to study the focusing on a structure for example), and should either be suppressed by an ad-hoc technique or at least taken into account through the data analysis.

Another interesting kind of simulation is the generation of a directional irregular wavefield. The wavefield simulated here is created from a Bretschneider spectrum with zero-crossing period $T_Z = 1.4$ s and significant wave height $H_s = 2$ cm. The

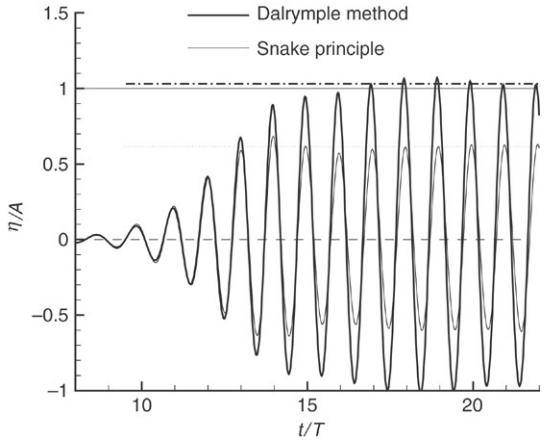

Fig. 12. Geometric focusing: probe located at the focusing point.

directional spreading used is $\cos^{2n}[(\theta - \theta_o)/2]$ with $n = 10$; 320 wave components are employed. The phases are adjusted so that all the components focus at the location ($x = 20$ m, $y = 15$ m) at $t = 80$ s. Following the conclusions drawn for the geometric focusing, the Dalrymple method is used to control the wavemaker. The mesh used in the simulation includes 256×128 nodes on the free surface and 128×32 nodes on the wavemaker. The whole simulation from which Fig. 13 is extracted covered 600 s real-time, for which 28 800 time-steps were necessary, corresponding to about 17 h CPU-time on a 3 GHz-Xeon single-processor PC. Fig. 13 shows two views of the free surface at $t = 80$ s when the wave packet is fully focused, on the left at first order and on the right at second order. It can be seen that the second-order component is much greater inside the focused wave packet than everywhere else in the random directional wave field, as expected since the bound waves are related to the square of the linear ones.

To further illustrate the behaviour of the numerical model with irregular waves, a comparison has been performed in the case of another long-time generation, this time of 2D irregular waves. Fig. 14 shows the wave-elevation history of a high-amplitude wave group within the 2D irregular wavefield, after 755 s real-time of generation (about 540 waves) for two steepnesses ε_c (defined here as the ratio of the significant wave height over the peak wavelength of the Bretschneider spectrum). The probe is located 20 m away from the wavemaker in a 50 m-long basin of depth 5 m. The comparison at the lower steepness $\varepsilon_c = 1.5\%$ shows a good agreement between the simulated wavefield and the experimental data, for the high-

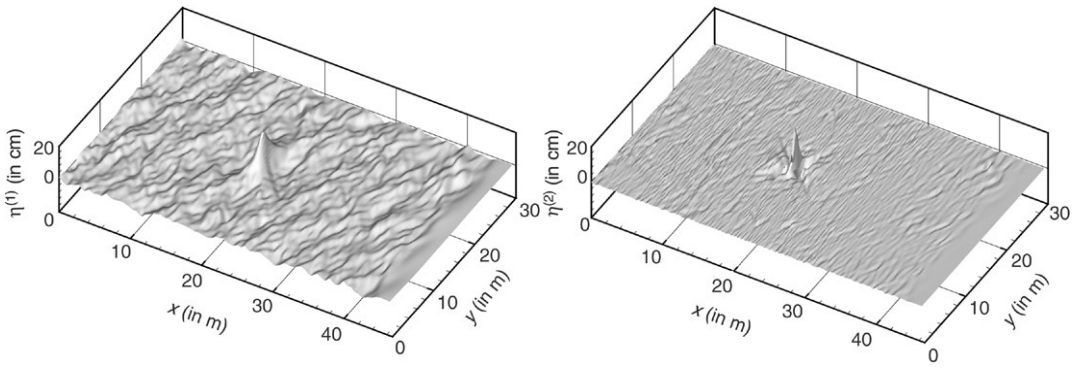

Fig. 13. Directional waves: first (left) and second (right) order elevations.

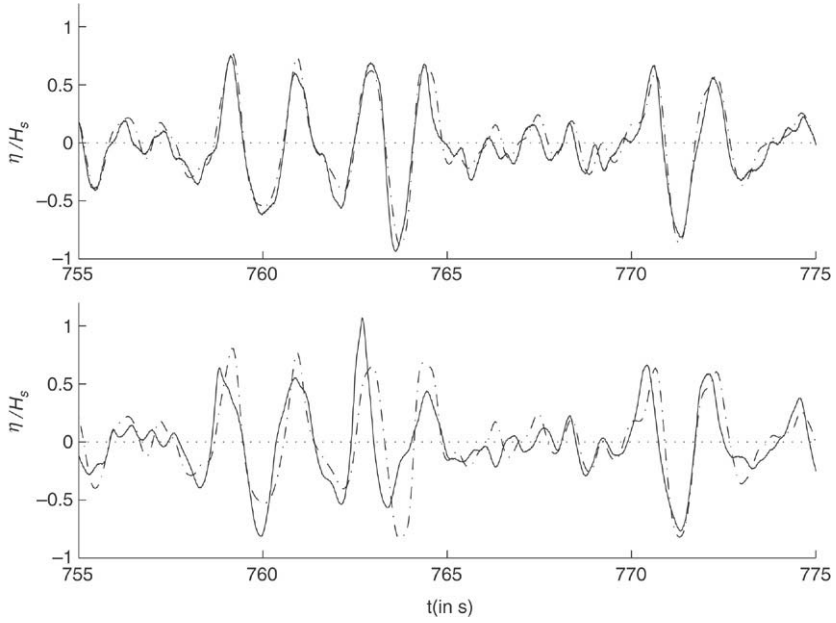

Fig. 14. 2D irregular-wave elevation history: comparison of experimental data (—) and second-order simulation (---). Top: $\varepsilon_c = 1.5\%$, bottom: $\varepsilon_c = 3\%$.

amplitude wave packet between $t = 760$ and 765 s as well as for the low-amplitude one in the range $765 < t < 770$ s. This emphasizes the ability of the model to simulate long-time evolutions in the wavetank, which confirms the quality of the wave generation process as well as the performance of the absorbing zone. The higher steepness studied $\varepsilon_c = 3\%$ illustrates, however, the limits of the model which fails to correctly reproduce the high-wave packets in this case. At this steepness, a model involving higher-order nonlinearities is required. This is why we have initiated the development of a fully-nonlinear version of our NWT model. This new model called *HOST* has already shown already encouraging first results (see e.g. [14]) and is presently under further development.

4. Conclusion

In this two-part paper, an efficient three-dimensional NWT model, named *SWEET*, has been presented, and its possibilities illustrated and discussed. In the first part (A) [1], the details of the fully-spectral methodology employed have been presented, modeling the time-domain formulation of the problem at second order. The originality of the proposed spectral scheme has been shown, allowing one to fully resolve the wavetank problem; classicaly, these spectral methods are limited to periodic unbounded domains. The resulting FFT-based algorithm has also been described in details. The numerical properties of the solver have then been verified. The latter exhibits the quick convergence and accuracy expected which, added to the fast resolution achieved by means of FFTs only, permit fine meshes at moderate costs (the overall cost is about $O(N \log_2 N)$ where N is the total number of nodes used). The consequence of this efficiency is the possibility of accurately reproducing the wavefield evolution in the wavetank, including the finest free-surface structures.

The latter capability has been verified in the present part (B) of the paper, by careful validations. First, the model has been successfully compared to a recent 3D steady-state semi-analytical solution [3] which accounts for both the wavemaker and sidewalls; exhibiting less than 2% error at second order with a not-so-fine mesh. In order to be able to further compare with experimental results for various cases, special efforts have

been dedicated to include in the model as many as possible of the features of the real basin. In particular, the arbitrary shape and motion of the real wavemaker have been accounted for (see [1]), and numerical and experimental wavemaker motions are identically constructed on the basis of a shared input process (see Section 2.1). In addition, dedicated experiments have been undertaken to adequately calibrate the numerical absorbing zone (see Section 2.2).

Thanks to the inclusion of all these features, our NWT is suitable for assisting the realization and analysis of wavetank experiments. This is illustrated by means of the numerical investigation of the usable test zone, knowledge of which is crucial to experiments. In particular, it has been shown how this usable test zone, enhanced at first order by derived linear-theory optimized wavemaker motions, is strongly degraded by free waves at second order; and further, how its extent reduces with time also at first order, due to partial reflection by the experimentally-calibrated numerical beach (see Section 3.1 and [2]). Among other examples of the aid to wavetank experiments provided by *SWEET* is the capability of optimizing the time ramp applied to the real wavemaker motion at the start (see Section 2.1).

The possibilities offered by the model have been further illustrated with the simulations of two- and three-dimensional complex wave patterns in the tank. The various cases shown have been carefully analyzed to determine both the model ability to reproduce real wavetank evolutions, and its limits in terms of nonlinearities and evolution durations. In particular, a very close agreement with experiments has been found for the cases of focused wave packets and long-time evolution of moderate-steepness irregular waves, showing the reliability of the numerical wave generation and propagation process as well as the performance of the absorbing zone (see Section 3.2). Three-dimensional geometric focusing and directional wavefield cases have also been investigated, demonstrating how the model can simulate long-time evolutions of realistic wavefields, with practical computational times of the order of 17 single-CPU hours for 600 s real-time simulated, with 32 000 nodes on the free surface and 4000 on the wavemaker (see Section 3.4). The variety of the model possibilities has also been illustrated through the example of the pre-design study of a partial lateral wavemaker for an existing towing tank (see Section 3.3).

The value of the present model *SWEET* has thus been demonstrated. Nonetheless, this model is presently formulated at second-order, which limits its application to moderate steepnesses. For steeper waves, such as in the higher irregular wavefield shown in the last example of application (Fig. 14), a model involving higher-order nonlinearities is required. In particular, the modification of the wave dispersion at third order has a decisive influence on the propagation of (non-breaking) realistic steep sea-patterns (see e.g. [14]). The natural development of the present model might therefore have been to extend it up to third order, which presents no theoretical difficulty. Nonetheless, due to the increased complexity of the expressions and the consequent numerical costs involved, we preferred to develop a fully-nonlinear spectral NWT model. This model, called *HOST* (standing for *Higher-Order Spectral wave Tank*), has already shown encouraging first results (see e.g. [17]), although the latter were obtained with a linear wave generation process only. Indeed, in [17] the linear part of the additional potential used in *SWEET* was included in the model to generate the waves, and it thus benefited from all of the features described here. Currently, ongoing work on this model includes nonlinear generation and an improved de-aliasing procedure for high steep waves. These new features will be reported in a complementary paper in the near future.

Finally, it should be mentioned that this kind of model will provide a useful tool in the framework of the wave-body interaction models based on the Spectral-Wave Explicit Navier–Stokes Equations (*SWENSE*), which are being developed in the authors' laboratory. The latter are powerful models that combine the accuracy of an arbitrary complex wavefield generated by a dedicated spectral potential-flow method, and the efficiency of a Navier–Stokes model solving only for the diffracted part of the field, efficiently limiting the viscous-flow computational domain to the vicinity of the body [18,19].

Appendix A. Directional wavemaker theory

We consider the generation of a regular wave of wavenumber k, complex amplitude $\underline{a}$ and direction θ in a basin semi-infinite in its main direction x, with perfectly reflective sidewalls located at $y = 0$ and $y = L_y$, and of constant depth h. The first-order elevation is the real part of the following implicit double summation

$$\eta^{(1)}(\vec{x}, t) = \underline{a_{mn}} \mathrm{e}^{-\mathrm{i}k_{mn}x} \cos(\mu_n y) \mathrm{e}^{\mathrm{i}\omega t}$$

where ω is the angular frequency linked to k by the dispersion relation $\omega^2 = gk \tanh kh$. The coefficients μ_n are the transverse natural wavenumbers of the basin, $\mu_n = n\pi/L_y$. The longitudinal wavenumbers k_{mn} are defined by $k_{mn}^2 = \alpha_m^2 - \mu_n^2$, where the vertical wavenumbers α_m are the solutions of $\omega^2 = g\alpha_m F^-(\alpha_m, h)$,[3] with $\alpha_\mathrm{o} = k$ and $\alpha_m \in \mathrm{i}\mathbb{R}^-$ for $m \geq 1$. The modal amplitudes $\underline{a_{mn}}$ are obtained by considering the wavemaker condition, and depend on the control law of the wavemaker. The following Appendix B expresses these coefficients for the Dalrymple method.

At second order, the elevation is the superimposition of the bound- and free-wave elevations. The former consists of the sum and difference terms

$$\eta_b^{(2)}(\vec{x}, t) = \underline{a_{mnpq}^{\pm}} \mathrm{e}^{-\mathrm{i}(k_{mn} \pm k_{pq})x} \cos[(\mu_n \pm \mu_q)y] \mathrm{e}^{2\mathrm{i}\omega t}$$

where the modal amplitudes $\underline{a_{mnpq}^{\pm}}$ are obtained by reporting the first-order expressions in the free-surface boundary conditions. And the free-wave elevation is given by

$$\eta_f^{(2)}(\vec{x}, t) = \underline{b_{mn}} \mathrm{e}^{-\mathrm{i}\gamma_{mn}x} \cos(\mu_n y) \mathrm{e}^{2\mathrm{i}\omega t}$$

[3] The function $F^{\pm}$ is defined by

$F^{\pm}(\alpha, z) = (\mathrm{e}^{\alpha z} \pm \mathrm{e}^{-\alpha z})/(\mathrm{e}^{\alpha} + \mathrm{e}^{-\alpha})$.

where $\gamma_{mn}^2 = \beta_m^2 - \mu_n^2$, and β_m is solution of $4\omega^2 = g\beta_m \; F^-(\beta_m, h)$. The modal amplitudes $\underline{b_{mn}}$ are obtained through the boundary condition on the wavemaker. The expressions for $\underline{a^{\pm}_{mnpq}}$ and $\underline{b_{mn}}$ are lengthy and thus not reproduced here; the reader can refer to [3] for more details.

Appendix B. Dalrymple method

The Dalrymple method [5] is an enhanced control law for the snake wavemaker in the case of the generation of a regular wave of complex amplitude $\underline{a}$, wavenumber k and direction θ. This method takes advantage of the reflective sidewalls to enlarge the usable zone. The wavemaker motion at the mean water level is given by

$$X_1(y,t) = \mathrm{Re}\,\underline{TF}\sum_{n=0}^{N_1}\underline{a_{on}}\cos(\theta_n)\cos(\mu_n y)\mathrm{e}^{\mathrm{i}\omega t}$$

with ω the angular frequency of the wave. $\underline{TF}$ stands for the 2D transfer function of the wavemaker, i.e. $\underline{TF} = \underline{s}/\underline{a}$ with $\underline{s}$ the complex stroke amplitude at the mean water level. The quantities $\underline{a_{on}}$, θ_n and μ_n are related to the 3D analytical solution of the wave generation problem. If we consider only the progressive modes, the linear free surface elevation can be written:

$$\underline{\eta_1}(\vec{x}) = \sum_{n=0}^{N_1}\underline{a_{on}}\cos(\mu_n y)\mathrm{e}^{-k_{on}x}$$

where N_1 is the integer part of kL_y/π, $\underline{a_{on}}$ the complex modal amplitude, and k_{on} the complex longitudinal wavenumbers. Then, θ_n is the direction of propagation associated with the nth mode, $\theta_n = \arcsin(\mu_n/k)$. Dalrymple assumes that this elevation fits a required ideal linear wave at a given distance $x = X_d$ from the wavemaker, so the complex amplitudes are

$$\underline{a_{on}} = \underline{a}\,I_n\mathrm{e}^{(k_{on}-k\cos\theta)X_d}$$

where

$$I_n = \frac{\int_0^{L_y}\mathrm{e}^{-\mathrm{i}k\sin\theta y}\cos(\mu_n y)\mathrm{d}y}{\int_0^{L_y}\cos^2(\mu_n y)\mathrm{d}y} = \begin{cases}\delta_{on} & \text{if } \theta = 0\\ 1 & \text{if } \theta \neq 0 \quad \text{and} \quad \mu_n = |k\sin\theta|\\ \dfrac{2ik\sin\theta}{(k\sin\theta)^2-\mu_n^2}\dfrac{\mathrm{e}^{-\mathrm{i}k\sin\theta L_y}(-1)^n-1}{L_y(1+\delta_{on})} & \text{else}\end{cases}$$

in which δ_{on} is the Kronecker symbol.

Appendix C. Separation of non linear components

Two focused wavefields are generated in the basin. The 'crest focused' group is first obtained with a given set of wave components to build the wavemaker motion. The second wavefield, 'trough focused', is the inverse of the former, obtained by using the same set of components but with amplitudes of opposite sign. The wave elevations at the focusing point are recorded in both cases, respectively giving η and η^*. Then the odd and even elevations are built by combinations: $\eta_{\mathrm{odd}} = (\eta - \eta^*)/2$ and $\eta_{\mathrm{even}} = (\eta + \eta^*)/2$.

The theoretical linear elevation can be written as the real part of

$$\eta^{(1)} = \sum_n \underline{a_n}\mathrm{e}^{\mathrm{i}(\omega_n t - k_n x)}.$$

Using these linear components, the odd and even elevations are given at third order by

$$\eta_{\mathrm{odd}} = \sum_n \underline{a'_n}\mathrm{e}^{\mathrm{i}(\omega_n t - k'_n x)} + \sum_{m,n,p}\underline{a_m}\underline{a_n^{\pm}}\underline{a_p^{\pm}}F_{mnp}^{\pm,\pm} \times \mathrm{e}^{\mathrm{i}[(\omega_m \pm\omega_n\pm\omega_p)t-(k'_m\pm k'_n\pm k'_p)x]} \quad \text{(C.1)}$$

$$\eta_{\mathrm{even}} = \sum_{m,n}\underline{a_m}\underline{a_n^{\pm}}G_{mn}^{\pm}\mathrm{e}^{\mathrm{i}[(\omega_m\pm\omega_n)t-(k'_m\pm k'_n)x]} \quad \text{(C.2)}$$

where $a'_n = a_n(1+A_n)$ and $k'_n = k_n(1+K_n)$ are the amplitudes and wavenumbers correct to the third order, and $G_{mn}^{\pm}$ and $F_{mnp}^{\pm,\pm}$ some appropriate coefficients which are independent of the linear amplitudes $\underline{a_n}$. The second order coefficients G_{mn} can be found e.g. in Dalzell [20]. The superscript $\pm$ denotes the sum and difference terms. The amplitudes $\underline{a_n^{\pm}}$ are respectively equal to $\underline{a_n}$ for the sum term $(+)$, and to its conjugate for the difference term $(-)$. Concerning the even elevation, one can notice that third-order nonlinearities are included in the term $k'_m \pm k'_n$ in (C.2), and thus modify the phase velocity of the sum and difference terms.

References

[1] Bonnefoy F, Le Touzé D, Ferrant P. A fully-spectral 3d time-domain model for second-order simultion of wavetank experiments. Part A: Formulation, implementation and numerical properties. Appl Ocean Res 2005 [submitted for publication]. doi:10.1016/j.apor.2006.05.004.

[2] Le Touzé D, Bonnefoy F, Ferrant P. Second-order spectral simulation of directional wave generation and propagation in a 3d tank. In: Proc. 12th int. offshore and polar engng. conf. vol. 3. 2002. p. 173–79.

[3] Bonnefoy F, Le Touzé D, Ferrant P. Second order wavemaker theory: prediction and control of free waves. In: Proc. 18th int. workshop on water waves and floating bodies. 2003.

[4] Biésel F. Wave machines. In: Proc. 1st conf. on ships and waves. 1954.

[5] Dalrymple RA. Directional wavemaker theory with sidewall reflection. J Hydraul Res 1989;27(1):23–4.

[6] Boudet L, Pérois J-P. Nouvelles techniques de pilotage d'un batteur segmenté pour la génération de houle oblique. In: C.R. 8èmes Journées de l'Hydrodynamique, JH8. 2001.

[7] Cointe R, Molin B, Nays P. Nonlinear and second-order transient waves in a rectangular tank. In: Proc. behavior of offshore structural systems conf. 1988.

[8] Le Touzé D. Méthodes spectrales pour la modélisation non-linéaire d'écoulements à surface libre instationnaires. Ph.D. thesis. France: École Centrale de Nantes; 2003.

[9] Stassen Y. Simulation numérique d'un canal à houle bidimensionnel au troisième ordre d'approximation par une méthode intégrale. Ph.D. thesis. France: École Centrale de Nantes; 1999.

[10] Hudspeth RT, Sulisz W. Stokes drift in two-dimensional wave flumes. J. Fluid Mech. 1991;230:209–29.

[11] Schäffer HA, Steenberg CM. Second-order wavemaker theory for multidirectional waves. Ocean Eng 2003;30(10):1203–31.

[12] Li W, Williams A. Second-order waves in a three-dimensional wave basin with perfectly reflecting sidewalls. J Fluid Struct 2000;14(4):575–92.

[13] Molin B. Numerical and physical wavetanks: Making them fit. Ship Tech Res 2001;48(1):2–22. 22nd Georg Weinblum Memorial Lecture.

[14] Bonnefoy F. Modélisation expérimentale et numérique des états de mer complexes. Ph.D. thesis. France: École Centrale de Nantes; 2005.

[15] Mansard E, Funke E. The measurement of incident and reflected spectra using a least squares method. In: Proc. 17th int. conf. on coastal engng. 1980. p. 154–72.

[16] Baldock TE, Swan C, Taylor PH. A laboratory study of nonlinear surface waves on water. Phil Trans Roy Soc Lond A 1996;354:649–76.

[17] Bonnefoy F, Le Touzé D, Ferrant P. Generation of fully-nonlinear prescribed wave fields using a high-order spectral method. In: Proc. 14th int. offshore and polar engng. conf. 2004.

[18] Ferrant P, Gentaz L, Alessandrini B, Le Touzé D. A potential/ranse approach for regular water wave diffraction about 2d structures. Ship Tech Res 2003;50(4):165–71.

[19] Luquet R, Alessandrini B, Ferrant P, Gentaz L. Simulation of the viscous flow past a ship in waves using the SWENSE approach. In: Proc. 24th ONR symp. on naval hydrodynamics. 2004.

[20] Dalzell J. A note on fintite depth second-order wave-wave interactions. Appl Ocean Res 1999;21:105–11.